

Vijay K. Dhir
e-mail: vdhir@seas.ucla.edu

Gopinath R. Warrier

Eduardo Aktinol

Mechanical and Aerospace
Engineering Department,
Henry Samueli School of
Engineering and Applied Science,
University of California, Los Angeles,
420 Westwood Plaza,
Los Angeles, CA 90095

Numerical Simulation of Pool Boiling: A Review

A review of numerical simulation of pool boiling is presented. Details of the numerical models and results obtained for single bubble, multiple bubbles, nucleate boiling, and film boiling are provided. The effect of such parameters such as wall superheat, liquid subcooling, contact angle, gravity level, noncondensables, and conjugate heat transfer are also included. The numerical simulation results have been validated with data from well designed experiments. [DOI: 10.1115/1.4023576]

Keywords: pool boiling, numerical simulation, prediction

1 Introduction

Boiling is one of the most efficient modes of heat transfer and as such is routinely used in applications such as power generation, propulsion, electronics cooling, chemical processes, etc. Over the past eight decades, significant progress has been made in improving our understanding of the boiling process. In spite of the progress made, we are still unable to accurately predict, from basic principles, the boiling curve.

Among the three modes of boiling—nucleate, transition, and film boiling, film boiling is most amenable to analysis. However, nucleate and transition boiling are much more complex processes and involve nonlinear interactions of several subprocesses. Numerous empirical correlations and mechanistic models have been proposed/developed to predict nucleate boiling [1–4]. Although the empirical correlations have served us well in the design of engineered systems, their predictive ability becomes suspect when applied to new situations. Also many of these correlations may be valid at the global level, but are rarely consistent at the subprocess level.

Mechanistic models of nucleate boiling have been developed to reduce the level of empiricism. These models [1,2], however, require knowledge of such parameters as number density of active sites, bubble diameter at departure, bubble release frequency, etc. However, because of the complexity and interactions of the involved subprocesses, we have had limited success in developing comprehensive models for nucleate boiling. This difficulty has in turn stifled further development of mechanism based models for predicting the heat transfer rate during nucleate boiling.

All the predictive methods (both empirical and mechanistic) mentioned above have almost exclusively focused on the mechanisms occurring on the fluid side. However, the solid heater surface and the heat transfer processes occurring on the fluid side are tightly coupled to heat conduction in the solid. For example, bubble waiting time, bubble release frequency, and heat transfer occurring at the bubble base and surrounding area are strongly dependent on the temperature distribution in the solid. Due to the complex interaction between the solid and fluid, we have not been able to incorporate simultaneously the heater's thermal response into the predictive models for nucleate boiling.

Dhir [4] has proposed the use of complete numerical simulations as an alternate method to predict the boiling curve. Advances in computing power and modeling techniques have resulted in high fidelity computer simulations. Numerical simulations have been shown to be successful in modeling single bubble, vertical merger and formation of vapor columns, lateral merger of bubbles and formation of mush-

room type bubbles, and nucleate and film boiling heat transfer. However, most of this work has been carried out under the assumption of constant wall temperature. As a result, the solid is thermally decoupled from the processes occurring on the fluid side.

Due to the fact that it is more amenable to analysis, we have had most success in developing correlations/models and numerical models to predict rate of heat transfer during film boiling [5–12].

During transition boiling, wall heat flux decreases as the wall superheat increases. This is an inherently unstable process which is manifested by intermittent liquid-solid and vapor-solid contact at a given location. Hence, conditions similar to nucleate boiling and film boiling prevail during the wet and dry periods, respectively. Consequently, the variation in heat flux with wall superheat is a function of the fraction of time a given area on the heater surface experiences each of the boiling modes. Hysteresis is observed during transition boiling; different curves are obtained depending on which side one approaches transition boiling from, nucleate boiling side or film boiling side [13–15]. The hysteresis is dependent on the surface wettability. Additionally, due to thermal inertia of the heater, the entire transition boiling region is often not accessible. Only with advanced feedback control systems has it been possible to even access the entire transition boiling region [16]. This mode of boiling is least studied and correlations/models currently available for prediction of transition boiling are not very robust.

In this work we will review the numerical models used to simulate pool boiling heat transfer. Thereafter, we will provide key numerical results obtained from such simulations and their validation with data from experiments.

2 Numerical Model

Four key subprocesses and their interactions need to be addressed if one is to develop a credible predictive model for nucleate boiling. These subprocesses (shown in Fig. 1) are (i) density of active nucleation sites, (ii) thermal response of heater, (iii) bubble dynamics—which includes bubble growth, merger, and departure, and (iv) heat transfer mechanisms such as transient conduction into liquid, evaporation at bubble base and boundary, thermocapillary convection resulting from surface-tension gradients along the interface, and convection induced by motion of vapor bubbles. In the following, we first discuss bubble dynamics and associated heat transfer. It is followed by a brief discussion of thermal response of the solid and active nucleation site density.

One of the earliest attempts to model bubble growth and departure from a heated wall was by Lee and Nydahl [17]. In this study the bubble growth rate was calculated by solving the two-dimensional axisymmetric Navier-Stokes and energy equations numerically to determine the associated flow and temperature fields. Due to the fact that they assumed a hemispherical bubble

Manuscript received November 18, 2012; final manuscript received January 14, 2013; published online May 16, 2013. Assoc. Editor: Leslie Phinney.

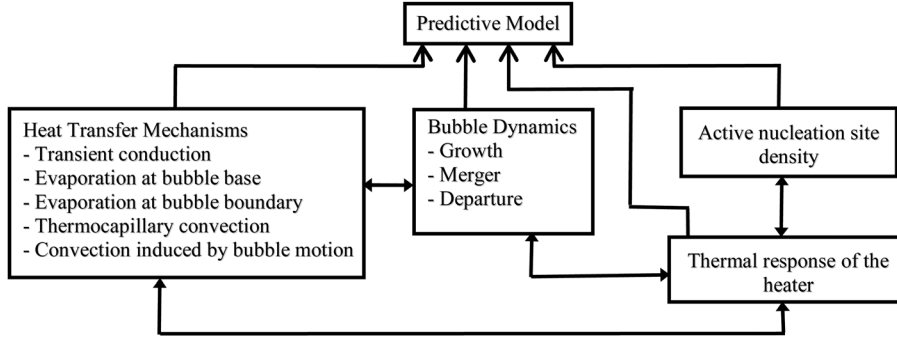


Fig. 1 Predictive model for nucleate boiling

and wedge shaped microlayer, they could not account for the change in bubble shape during growth. The wall temperature was assumed to be constant. Cooper and Lloyd's [18] formulation was used for the microlayer thickness.

Mei et al. [19] studied the bubble growth and departure time using numerical simulations. They assumed that a wedge shaped microlayer existed underneath the bubble and that the heat transfer to the bubble was only through the microlayer. This assumption is not totally correct for both subcooled and saturated boiling. The study did not consider the hydrodynamics of the liquid motion induced by the growing bubble and introduced empiricism through the shape of the growing bubble. However, in their work the temperature distribution in the heater was solved for numerically.

Welch [20] studied bubble growth using a finite volume method and an interface tracking method. Conduction in the solid wall was accounted for, but the microlayer was not modeled explicitly. The first complete numerical simulation of bubble growth was performed by Son et al. [21]. In their study, in addition to the solution of the conservation equations, the liquid-vapor interface was captured using the level-set (LS) method. This level-set method had been previously applied to adiabatic incompressible two-phase flow by Sussman et al. [22] and to film boiling near critical pressures by Son and Dhir [6]. In the model of Son et al. [21], the computational domain was divided into two regions, namely, the micro region and the macro region as shown in Fig. 2. The micro

region is the ultrathin liquid film that forms between the solid surface and the evolving liquid-vapor interface. On the inner edge, the microlayer has a thickness of the order of a few nanometers (few molecules of liquid adsorbed on the surface and do not evaporate). The thickness of the nonevaporating (adsorbed) film depends on the vapor pressure, substrate temperature, and the disjoining pressure [23–25]. As such, the solid surface further radially inward is considered to be "dry" (i.e., nonevaporating microlayer). On the other hand, at the outer edge, the microlayer has a thickness of the order of several microns. Heat is conducted across this film and is utilized for evaporation. Lubrication theory similar to that developed by Wayner [23,24], Stephan and Hammer [26], and Lay and Dhir [27] was used to solve for the radial variation of microlayer thickness.

The equation of mass conservation in the microlayer used by Son et al. [21] is written as

$$\frac{\partial \delta}{\partial t} = v_l - \frac{q}{\rho_l h_{fg}} \quad (1)$$

In Eq. (1), the liquid velocity normal to the vapor-liquid interface v_l is obtained from the continuity equation as

$$v_l = -\frac{1}{r} \frac{\partial}{\partial r} \int_0^\delta r u_l dy \quad (2)$$

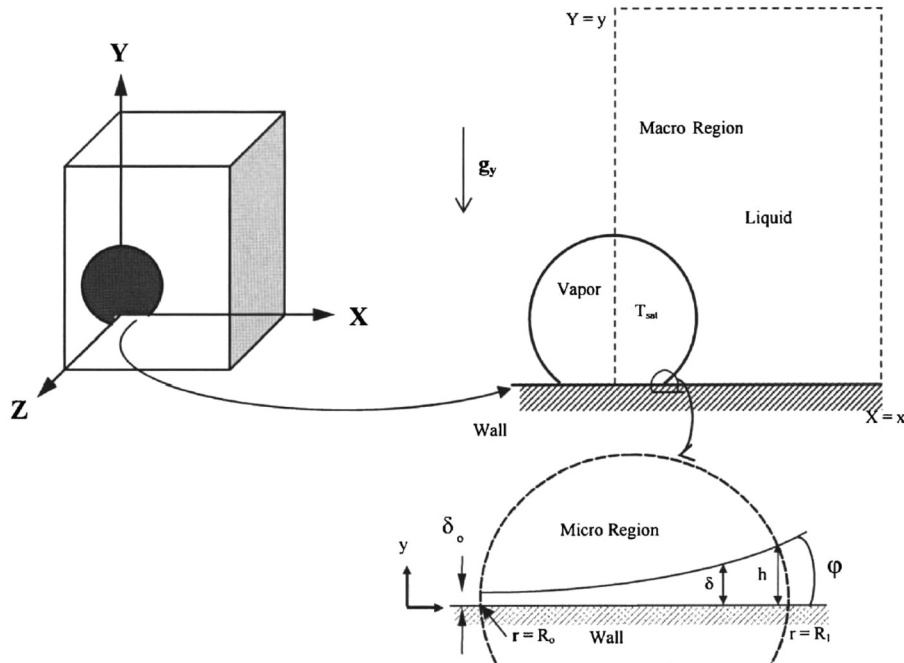


Fig. 2 Computational domain used in numerical simulations

Using lubrication theory, the momentum equation for the micro-layer is written as

$$\frac{\partial p_l}{\partial r} = \mu_l \frac{\partial^2 u_l}{\partial y^2} \quad (3)$$

The energy conservation equation for the film yields

$$q = k_l \frac{(T_w - T_{int})}{\delta} \quad (4)$$

Using the modified Clausis–Clayperon equation, the evaporative heat flux is written as

$$q = \frac{k_l(T_w - T_{int})}{\delta} = h_{ev}[T_{int} - T_v + (p_l - p_v)T_v/\rho_l h_{fg}] \quad (5)$$

where

$$h_{ev} = \left(\frac{2M}{\rho R T_v} \right)^{1/2} \frac{\rho_v h_{fg}^2}{T_v}; \quad T_v = T_{sat}(p_v) \quad (6)$$

The pressures in the vapor and liquid phases are related as

$$p_l = p_v - \sigma\kappa - \frac{A}{\delta^3} + \frac{q^2}{\rho_v h_{fg}^2} \quad (7)$$

where σ was taken to be a function of temperature, and A is the dispersion constant relating disjoining pressure to the film thickness. In Eq. (7) the second term on the right-hand side accounts for the capillary pressure, the third term for the disjoining pressure, and the last term originates from the recoil pressure. The curvature of the interface is defined as

$$\kappa = \frac{1}{r} \frac{\partial}{\partial r} \left[r \frac{\partial \delta}{\partial r} \sqrt{1 + \left(\frac{\partial \delta}{\partial r} \right)^2} \right] \quad (8)$$

The combination of the mass, momentum, and energy equations for the microlayer yields

$$\delta''' = f(\delta, \delta', \delta'', \delta''') \quad (9)$$

where ' denotes $\partial/\partial r$. The boundary conditions for Eq. (9) are as follows:

$$\delta = \delta_0; \quad \delta' = \delta''' = 0 \text{ at } r = R_0 \quad (10)$$

$$\delta = h/2; \quad \delta'' = 0 \text{ at } r = R_1 \quad (11)$$

where δ_0 is of the order of molecular size, $h/2$ is the distance to the first computational node for the level-set function (ϕ) from the wall, and φ is an apparent contact angle that is measurable experimentally. In implementing the above boundary conditions, the radius R_1 was determined from the solution of the macro region. For a given contact angle, the microlayer formulation Eq. (9) is integrated using five boundary conditions Eqs. (10) and (11) under the condition that for a given dispersion constant R_0 and R_1 are unknown. The apparent contact angle is defined as

$$\tan \varphi = h/2/(R_1 - R_0) \quad (12)$$

For numerically analyzing the macro region, the level set formulation modified by Son et al. [21] to accommodate the effect of phase change is used. The interface separating the two phases is captured by the level-set function (ϕ), which is defined as a signed distance from the interface. The negative sign is chosen for the vapor phase and positive sign for the liquid phase. The equations

governing conservation of momentum, energy, and mass for the vapor-liquid region are written as

$$\rho \left(\frac{\partial \vec{u}}{\partial t} + \vec{u} \cdot \nabla \vec{u} \right) = -\nabla p + \rho \vec{g} - \rho \beta_T (T - T_{sat}) \vec{g} - \sigma \kappa \nabla H + \nabla \cdot \mu \nabla \vec{u} + \nabla \cdot \mu \nabla \vec{u}^T \quad (13)$$

$$\rho c_{pl} \left(\frac{\partial T}{\partial t} + \vec{u} \cdot \nabla T \right) = \nabla \cdot k \nabla T \text{ for } H > 0 \\ T = T_{sat}(p_v) \text{ for } H = 0 \quad (14)$$

$$\nabla \cdot \vec{u} = -\frac{1}{\rho} \left(\frac{\partial \rho}{\partial t} + \vec{u} \cdot \nabla \rho \right) + \dot{V}_{micro} = \frac{\vec{m}}{\rho^2} \cdot \nabla \rho + \dot{V}_{micro} \quad (15)$$

where

$$\rho = \rho_v + (\rho_l - \rho_v)H, \quad \mu^{-1} = \mu_v^{-1} + (\mu_l^{-1} - \mu_v^{-1})H, \quad k^{-1} = k_l^{-1}H \\ H = 1 \text{ if } \phi > 0 \text{ (liquid)} \\ H = 0 \text{ if } \phi < 0 \text{ (vapor)} \quad (16)$$

where h is the grid spacing and H is the Heaviside function. The volume source term included in Eq. (15) due to liquid-vapor phase change is derived from the conditions of the mass continuity and energy balance at the interface:

$$\vec{m} = \rho(\vec{u}_{int} - \vec{u}) = k \nabla T / h_{fg} \quad (17)$$

In Eq. (15) \dot{V}_{micro} is obtained from the microlayer solution as

$$\dot{V}_{micro} = \int_{R_0}^{R_1} \frac{k_l(T_w - T_{int})}{\rho_v h_{fg} \delta} r dr \quad (18)$$

where ΔV_{micro} is a vapor-side control volume near the micro region. In the level set formulation, ϕ is advanced and reinitialized as

$$\frac{\partial \phi}{\partial t} = -\vec{u}_{int} \cdot \nabla \phi \quad (19)$$

$$\frac{\partial \phi}{\partial t} = \frac{\phi_0}{\sqrt{\phi_0^2 + h^2}} (1 - |\nabla \phi|) \quad (20)$$

where ϕ_0 is a solution of Eq. (19). The length, velocity, and time scales used to normalize the governing equations are defined as

$$l_o = \sqrt{\frac{\sigma}{g(\rho_l - \rho_v)}}, \quad u_o = \sqrt{gl_o}, \quad t_o = \frac{l_o}{u_o} \quad (21)$$

For example, for water at earth normal gravity and 1 atm pressure, the length and time scales are $l_o = 2.5$ mm and $t_o = 16$ ms, respectively. The boundary conditions for the governing equations in two dimensions for the macro region are as follows.

At the wall ($y = 0$):

$$u = v = 0; \quad T = T_w; \quad \frac{\partial \phi}{\partial y} = -\cos \varphi \quad (22)$$

At the planes of symmetry ($r = 0, R$):

$$u = \frac{\partial v}{\partial r} = \frac{\partial T}{\partial r} = \frac{\partial \phi}{\partial r} = 0 \quad (23)$$

At the top of computational domain (free surface, $y = Y$):

$$\frac{\partial u}{\partial y} = \frac{\partial v}{\partial y} = \frac{\partial \phi}{\partial y} = 0; \quad T = T_{sat} \quad (24)$$

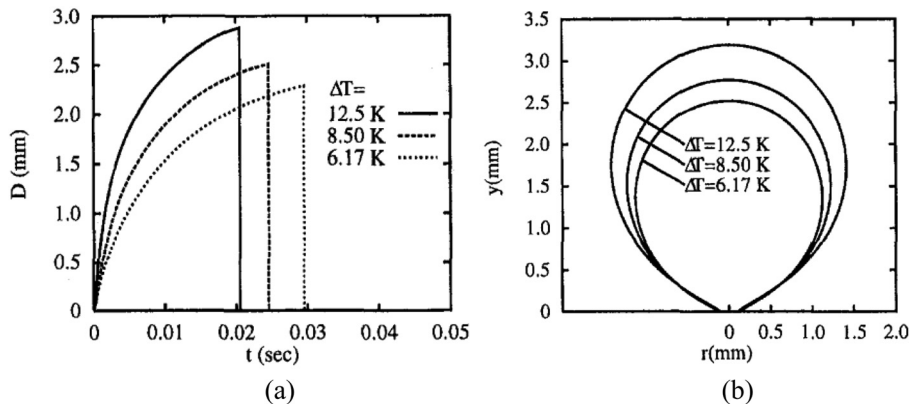


Fig. 3 Effect of wall superheat on bubble growth: (a) growth history and (b) bubble shape at departure for saturated water at $\varphi = 38$ deg (from [21])

During the computations, time steps were chosen to satisfy the CFL condition $\Delta t \leq h/[|u| + |v|]$. This was done because of the explicit treatment of the convection terms and the condition that the numerical results should change little if the time steps are halved. When bubbles merge in the lateral direction we carry out numerical simulations in three dimensions. However, for the microlayer contribution we continue to employ a two-dimensional model under the assumption of axisymmetry around a bubble.

In analyzing the micro region, continuum assumption was considered to hold until the film is a few molecules thick. Long-range forces are evaluated through the Hamaker constant, which is also related to the static contact angle; the value of the Hamaker constant is determined iteratively such that the desired apparent contact angle is obtained [21,27] (see Eq. (12)). The thickness of the adsorbed film (δ_o) is assumed to be 10^{-9} m (1 nm) in all cases, based on the work of Lay and Dhir [27], who found the effect of varying δ_o (varied from 9×10^{-10} to 10^{-8} m) to be negligible. The use of the static contact angle was justified based on the experimental results obtained by Ramanujan and Dhir [28], which showed only a ± 5 deg difference between the advancing and receding contact angles during pool boiling. In the microlayer formulation, capillary pressure gradient is related to change in the curvature and/or change in temperature of the interface and recoil pressure resulting from the momentum of vapor leaving the interface being higher than the liquid approaching the interface is included. Inertia terms are neglected in the momentum equation, and convection terms are ignored in the energy equation. Quasi-static analysis is carried out, and a two-dimensional model for the microlayer is used even in three-dimensional (3D) situations under the assumption that no crossflow occurs in the azimuthal direction.

For the macro region, the fluid is assumed to be incompressible. Additionally, the flows are assumed to be laminar, and all properties are evaluated at the mean temperature. The vapor is assumed to remain at saturation temperature corresponding to the pressure in the bubble. As such, the energy equation is not solved inside the vapor bubble and heat transfer from solid to vapor is ignored. A finite difference scheme is used to discretize the governing equations. All diffusion terms are solved implicitly, while the convection terms are solved explicitly. The projection method is used to solve for pressure. In order to increase the rate of convergence of the Poisson equation for pressure, the multigrid method is used. A second-order ENO scheme is adopted for the advection terms when solving for the level-set function. In the original model developed by Son et al. [21], the heater wall was maintained at a constant temperature, and symmetry conditions were imposed on the domain boundaries. The efficiency of the model was tested with several standard problems.

3 Numerical Simulation Results

3.1 Single Bubble Dynamics

3.1.1 Effect of Wall Superheat and Liquid Subcooling. Numerical simulation results of Son et al. [21] showed good agreement with data from experiments with respect to time-dependent vapor bubble shape, growth rate, bubble departure diameter, and growth period. The effect of increase in wall superheat was to increase the growth rate and bubble departure diameter but reduce the bubble growth period. This is consistent with the experimental data. The higher growth rate was due to increased heat transfer at the vapor-liquid interface, whereas the increase in departure diameter was due to the increased contribution of liquid inertia. Figure 3 shows the effect of wall superheat on a growing bubble for water at 1 atm pressure. Singh and Dhir [29] modified Son et al.'s [21] original formulation to include liquid subcooling effects. With the increase in liquid subcooling, the bubble growth rate decreases and growth period increases, while the bubble diameter at departure decreases.

3.1.2 Effect of Contact Angle. The effect of fluid properties, surface wettability, and contact angle on the bubble dynamics and heat transfer was investigated by Abarajith and Dhir [30]. Both the bubble departure diameter and the growth period for PF-5060 are much smaller than those for water. As seen in Fig. 4(a), the numerical predictions compare well with the experimental data for the two fluids. Figure 4(b) shows the results of numerical simulations carried out by parametrically varying the contact angle for the two liquids. When the bubble departure diameter and growth period, normalized with their corresponding values for a contact angle of 90 deg, is plotted as shown in Fig. 4(b), the data for both fluids nearly overlap. Bubble diameter at departure is seen to decrease linearly as the contact angle is reduced up to about 20 deg. This behavior is similar to that predicted from Fritz's correlation [31]. However, for contact angles less than 20 deg, when the surface becomes well wetting, the dependence of bubble departure diameter on contact angle is nonlinear. The growth period shows nonlinear behavior for all contact angles.

This model was later used to simulate a single bubble during pool boiling of water from a superhydrophilic surface $\varphi = 10$ deg [32]. Figure 5 shows a comparison of the numerical predictions and experimental data for bubble growth of water at various contact angles ($\varphi = 10$ deg, and 50 deg) at atmospheric pressure and $g/g_e = 1$. As contact angle increases, both the bubble departure diameter and the bubble growth time increase.

The wall heat transfer rates as well as the contributions of the various heat transfer mechanisms vary spatially and temporally during the bubble growth and departure cycle. Figure 6 shows the area-averaged wall heat flux and contributions of individual

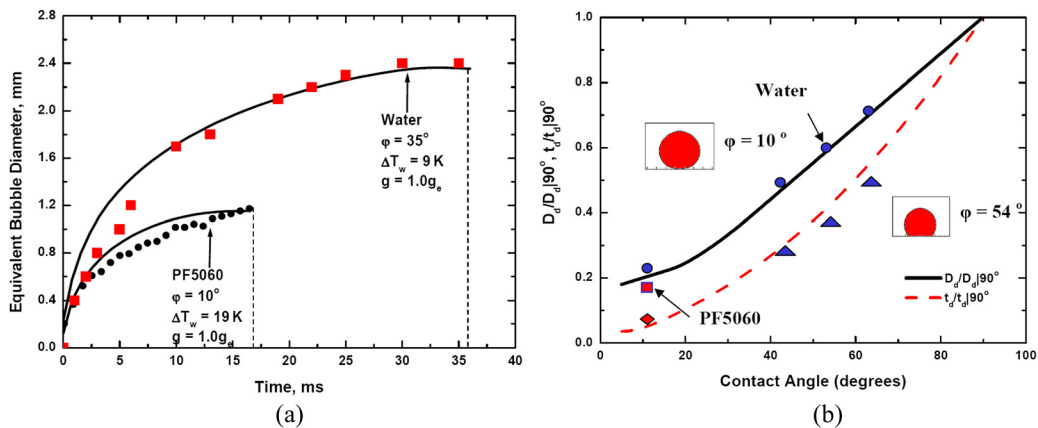


Fig. 4 (a) Growth rates for water and PF-5060 and **(b)** normalized departure diameter and growth time ($\Delta T_w = 8^\circ\text{C}$, $\Delta T_{\text{sub}} = 0^\circ\text{C}$, $g/g_e = 1.0$, from [30])

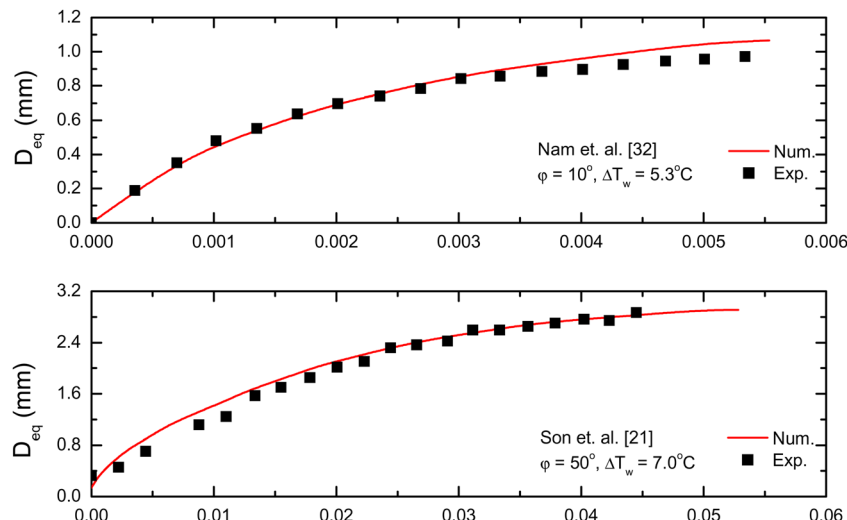


Fig. 5 Comparison of numerically predicted bubble growth for water for various contact angles

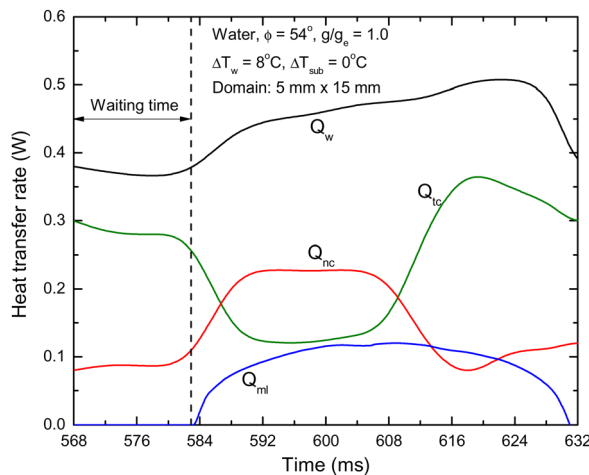


Fig. 6 Contributions of the various heat transfer mechanisms (from [30])

mechanisms as a function of time. Transient conduction dominates the area around the cavity during the waiting period ($t_w = 16\text{ ms}$). Thereafter its contribution decreases during the early growth period, but then again increases as the bubble base shrinks

during the detachment phase. Natural convection contribution is highest during the early growth period of the bubble when liquid is pushed out radially. Microlayer evaporation contributes only during the period in which the bubble is attached to the heater surface. Heat transfer rate from the heater surface peaks just before the vapor bubble lifts off from the heater. Time integrated values suggest that about 50% of the energy from the wall is transferred by transient conduction, 35% by natural convection and 15% by microlayer evaporation.

Partitioning of wall energy into vapor and liquid as determined from numerical simulations is shown in Fig. 7, for one growth and departure cycle of a bubble. The rate at which energy is utilized for vapor production is highest when the vapor bubble base diameter is nearly at its maximum. Conversely, this corresponds to the lowest energy transfer rate into superheating of the liquid. Time integrated values suggest that about 30% of energy from the wall is utilized in vapor production, whereas 70% goes into superheating of liquid.

3.1.3 Effect of Noncondensables. Wu and Dhir [33] investigated single bubble dynamics and heat transfer during subcooled pool boiling in the presence of noncondensables. In addition to the mass, momentum, and energy equations, the species conservation equation was also solved. The species conservation equation can be written as

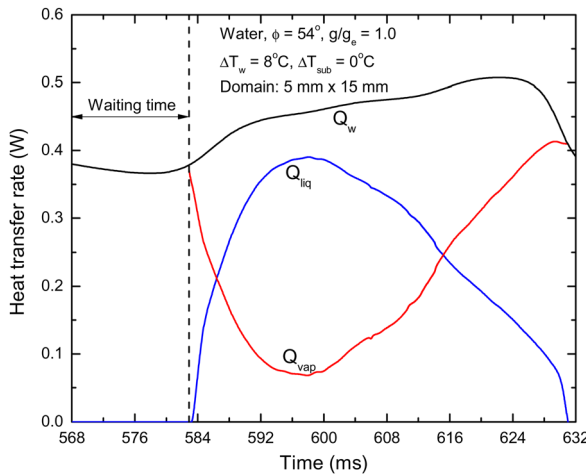


Fig. 7 Variation of heat transfer rate from the wall to liquid and vapor as a function of time (from [30])

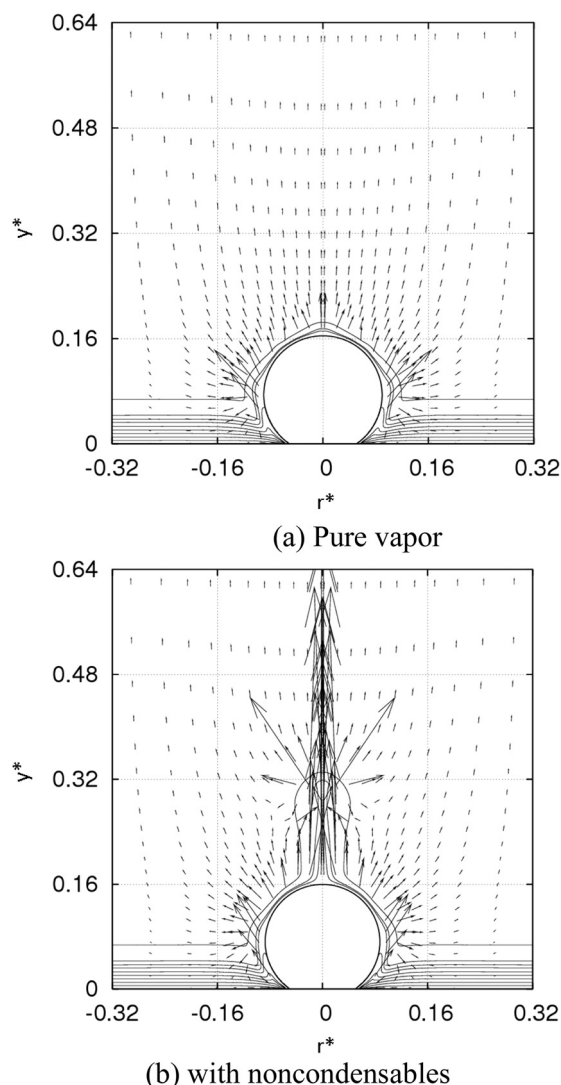


Fig. 8 Comparison of temperature and flow field for (a) pure vapor and (b) with noncondensables (fluid: water, wall superheat = 8.0 °C, liquid subcooling = 5.0 °C, $g/g_e = 10^{-4}$, $C_{g,0} = 0.2$, $C_{g,l} = 2.48 \times 10^{-6}$, from [33])

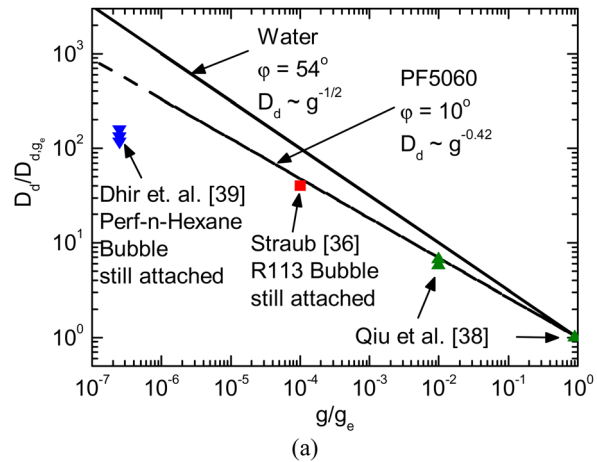


Fig. 9 The dependence of (a) bubble departure diameter and (b) growth period on gravity level

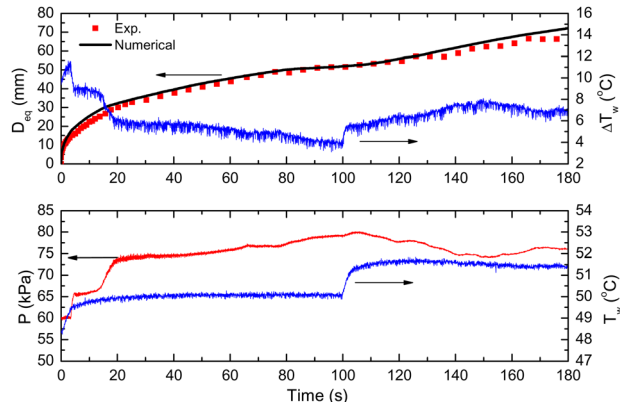


Fig. 10 Comparison of single bubble growth data with results from numerical simulations (from [39])

$$\rho \left(\frac{\partial C_g}{\partial t} + \vec{u} \cdot \nabla C_g \right) = \nabla \cdot \rho D \nabla C_g \quad \text{for } H \leq 0$$

$$C_g = C_{g,l} \quad \text{for } H > 0 \quad (25)$$

The saturation temperature inside the bubble and along the interface is then adjusted,

$$T = T_{\text{sat}}(p_v) = T_{\text{sat},x_g=0} + x_g \frac{\bar{R} T_{\text{sat},x_g=0}^2}{M h_{fg}} \quad \text{for } H \leq 0 \quad (26)$$

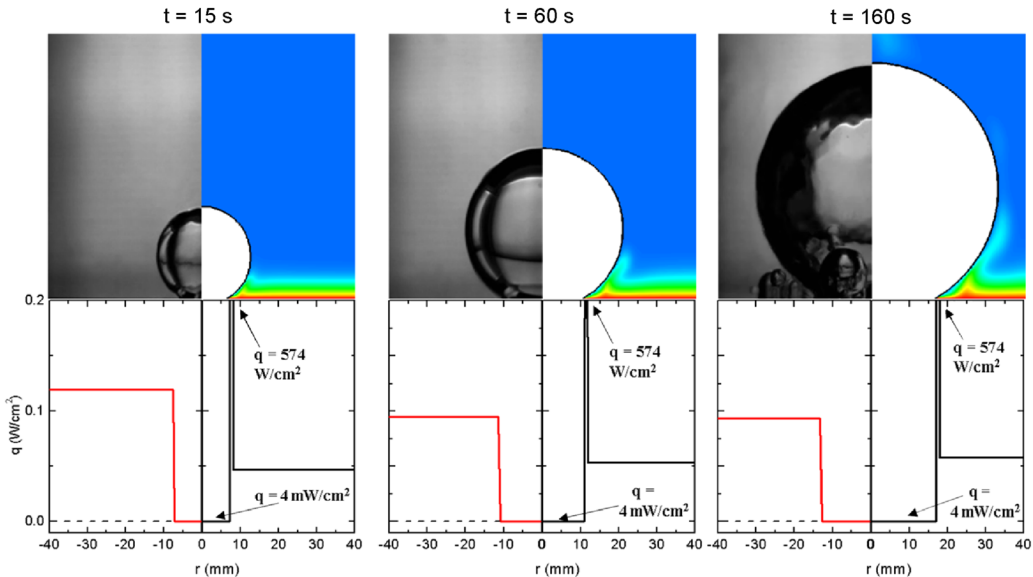


Fig. 11 Comparison of experimental data with results from numerical simulations (from [39])

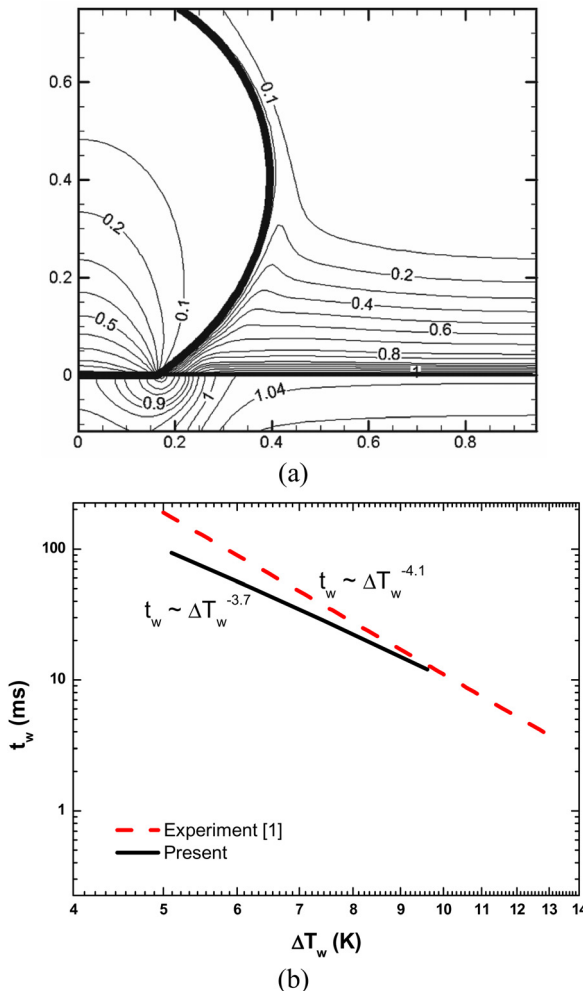


Fig. 12 (a) Isotherms for water boiling on stainless steel (0.3 mm thick, $q_w = 1.1 \text{ W/cm}^2$) and (b) comparison of numerical results and experimental correlation for bubble waiting time (copper, 1 mm thick, $q_w = 0.5$ to 2.0 W/cm^2 , from [44])

Mass conservation at the bubble interface yields

$$\begin{aligned} \rho D \nabla C_g &= -C_g \frac{k \nabla T}{h_{fg}} && \text{for condensation} \\ \rho D \nabla C_g &= -\frac{C_g - C_{g,l}}{1 - C_{g,l}} \frac{k \nabla T}{h_{fg}} && \text{for evaporation} \end{aligned} \quad (27)$$

The adaptive moving mesh method developed earlier by Wu et al. [34] was used in this study. The wall temperature was maintained constant. In this method, the total number of grid points is fixed but the grid automatically moves and adapts itself to the liquid-vapor interface during bubble growth and departure. Using such a grid, the interfacial heat transfer could be calculated accurately with significantly less grid points. The conservation equations were solved for both the liquid and vapor phases. The saturation temperature at the liquid-vapor interface was calculated using the local partial pressure of the vapor and as a result it varies along the bubble interface. The effect of increasing noncondensable concentration results in a larger bubble. This trend is not significant at Earth's normal gravity, but becomes more substantial as the gravity level decreases or the bubble growth time increases. The effect of noncondensables on the overall wall heat transfer rate was found to be negligible. No discernible change was seen in the flow and temperature field at Earth's normal gravity. However thermocapillary convection becomes more significant at reduced gravity levels and results in upward flow of liquid from the top of the bubble. Figure 8 shows a comparison of the flow and temperature field for the cases without and with noncondensables. Note that in Fig. 8 $C_{g,0}$ is the initial concentration in the bubble and $C_{g,l}$ is the gas concentration in the bulk liquid.

3.1.4 Effect of Gravity Level. Since buoyancy is one of the primary driving forces in the boiling process, any change in the gravitational force has a direct impact on the bubble dynamics. Numerous investigators have studied the effect that reducing gravity level has on bubble dynamics and heat transfer during boiling [35–39]. Fritz's correlation [31], which balances buoyancy and surface tension forces, predicts that the bubble departure diameter (D_d) would vary with gravity as $D_d \sim g^{-1/2}$. This prediction was corroborated by the numerical investigations of Abarajith et al. [40] and Zhao et al. [41].

Figure 9(a) shows the numerical predictions for bubble departure diameter as a function of gravity level for water with a contact angle of 54 deg and PF5060 with a contact angle of 10 deg

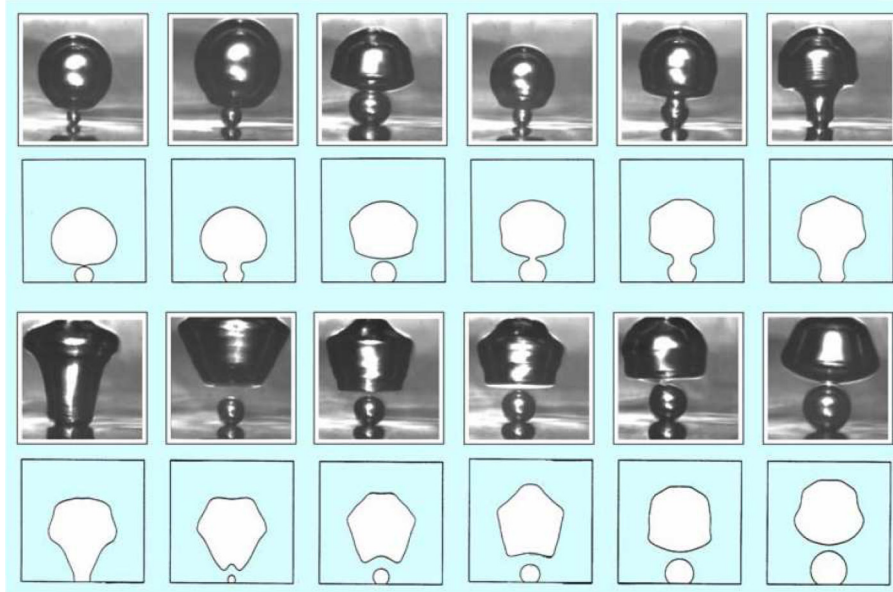


Fig. 13 Comparison of numerical and experimental bubble shapes during vertical merger (fluid: saturated water, $\Delta T_w = 10^\circ\text{C}$, $g/g_e = 1.0$, $\varphi = 38$ deg, from [46])

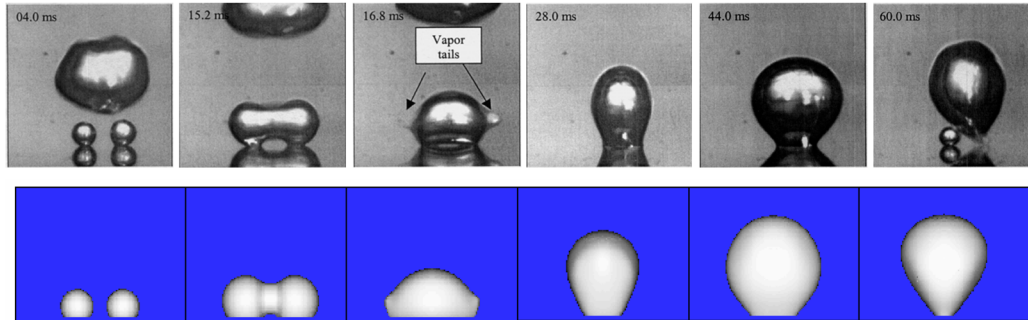


Fig. 14 Comparison of numerical and experimental bubble shapes during lateral merger (fluid: saturated water, $\Delta T_w = 5^\circ\text{C}$, $g/g_e = 1.0$, $\varphi = 38$ deg, spacing = 1.5 mm, from [47])

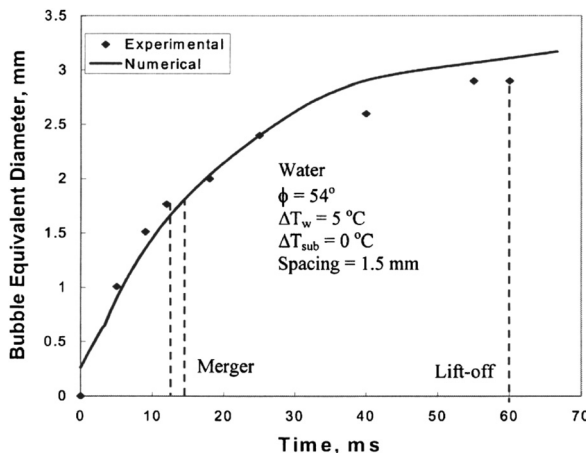


Fig. 15 Comparison of numerically predicted bubble growth with experimental data (from [47])

obtained by Abarajith et al. [40]. Included in the figure are experimental data of Qiu et al. [38], Straub [36], and Dhir et al. [39]. Experimental data are in agreement with the numerical predictions and do not contradict the predictions when bubbles are still

attached to the solid surface. Figure 9(b) shows the numerical predictions for growth period as a function of gravity level; available experimental data are also included. The numerical simulations tend to overestimate the limited experimental data available at low gravity levels. According to numerical simulations, $D_d \propto g^{-0.5}$, and $t_d \propto g^{-0.9}$.

Very recently Dhir et al. [39] simulated single bubble growth in microgravity conditions (fluid: perfluoro-*n*-hexane, $g/g_e \sim 10^{-7}$). Quantitative data of bubble equivalent diameter is plotted as a function of time in Fig. 10(a). The variation of wall superheat with time is also shown. Figure 10(b) shows the variation of system pressure and wall temperature during the bubble growth. In the numerical simulations, the area-averaged heater surface temperature, system pressure, and liquid temperature, as a function of time, were given as input. The solid line shows the prediction from numerical simulations of bubble equivalent diameter as a function of time. However, it was assumed that gas concentration in the vapor space was given by Henry's law. The interface temperature was the saturation temperature corresponding to the partial pressure in the vapor. The numerical model accounted for condensation at the upper part of the bubble and presence of dissolved gas in the liquid [33]. The energy equation was solved in the vapor region. The prediction from numerical model is in remarkably good agreement with data. Figure 11 compares at different times the bubble shape and heat flux under the bubble and surround area predicted from numerical simulations with those

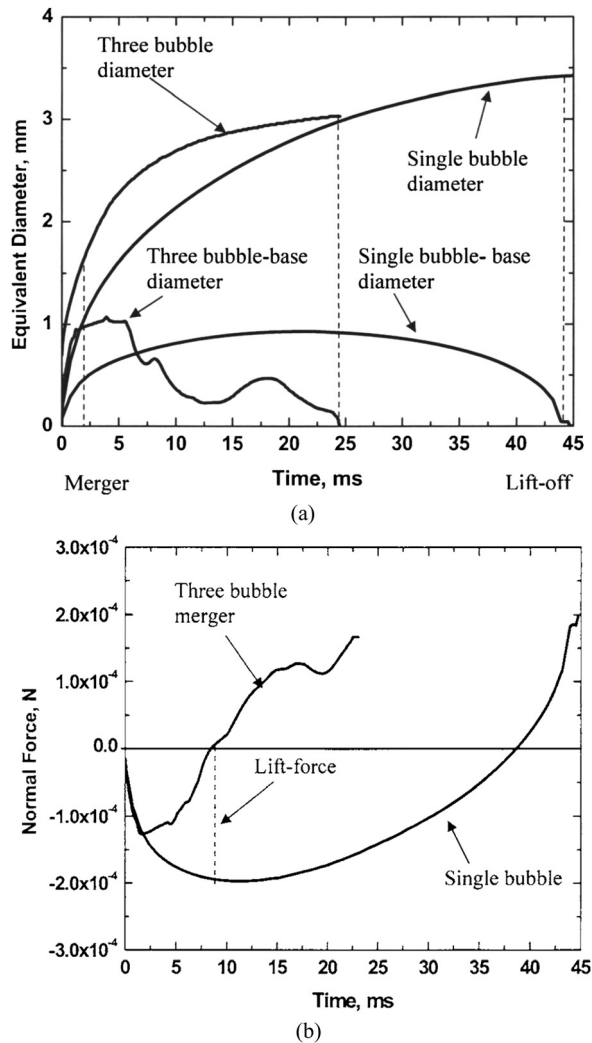


Fig. 16 Comparison of single bubble and three inline bubbles (a) bubble growth and (b) forces acting in the vertical direction (fluid: saturated water, $\Delta T_w = 10^\circ\text{C}$, $g/g_e = 1$, $\varphi = 54^\circ$, spacing = 1.25 mm, from [40,48])

observed in the experiments. It is found that numerical simulations do a good job in predicting bubble shape and size. In the experiments, due to the fact that the spatial resolution is not fine enough, the heat flux under the bubble cannot be determined when the bubble base is small. The results of numerical simulations show that the heat flux at the bubble base is very small (approximately $4 \times 10^{-3} \text{ W/cm}^2$). Note that the dry area under the bubble base begins from the inner edge of the microlayer. During the early period of bubble growth, experimentally observed heat flux on bubble unoccupied area of the heater is about two times that obtained from numerical simulations but at later periods the predicted heat fluxes are comparable to those observed in experiments. The numerical model shows a peak in heat flux near the triple point. This peak is not observed in the experiments because of lack of availability of fine resolution heat transfer data.

3.1.5 Conjugate Heat Transfer. Kunkelmann and Stephan [42,43] investigated single bubble dynamics and heat transfer during pool boiling of refrigerant HFE-7100. Conjugate heat transfer was modeled with the liquid-vapor interface being captured using the volume-of-fluid (VOF) method. Although only one bubble growth and departure cycle was simulated, the results showed a drop in temperature near the triple point during bubble growth; this was due to the high rate of evaporation contributed by the microlayer. A similar study was performed by Aktinol and Dhir

[44]. Several bubble growth and departure cycles were simulated. The nucleation criterion was based on the study of gas entrapment and surface wettability performed by Wang and Dhir [45]. Surfaces of different materials and thicknesses were studied. The isotherms in the fluid and solid phases for water boiling on 0.3 mm thick stainless steel disk can be seen in Fig. 12(a); the imposed heat flux is 1.1 W/cm^2 . The largest temperature drop on the solid side during bubble growth can be seen to be near the triple point. Figure 12(b) shows the waiting time as a function of wall superheat. The numerical prediction is in good agreement with the experimental results of Basu et al. [1]. The wall thickness for the data shown in Fig. 12(b) is 1 mm (material: copper); the imposed heat flux varies from 0.5 to 2.0 W/cm^2 .

3.2 Multiple Bubble Merger

3.2.1 Vertical Bubble Merger and Formation of Vapor Columns. At a given nucleation site, increase in the wall superheat results in an increase in bubble release frequency. When the growth rate of a bubble formed at the nucleation site exceeds the rate at which the lower interface of the preceding bubble moves away from the heater surface, bubble merger occurs in the vertical direction [46]. After merger, the combined vapor mass may detach from the heater surface before the process repeats itself. In performing these simulations, the bubble waiting time was varied parametrically as the conjugate heat transfer problem was not solved (i.e., wall superheat is specified). Figure 13 shows the results of visual observations and those from numerical simulations for one cycle of the merger of three consecutive bubbles in the vertical direction. The upper set of frames is from visual observations, whereas the lower set of frames is results from numerical simulations. The individual frames in each figure are from left to right and from top to bottom. After the merger of the departed bubble with the succeeding bubble, the larger vapor mass causes the vapor bubble at the nucleation site to prematurely depart. Thereafter, the second succeeding bubble merges with the vapor mass hovering over the surface. The combined vapor mass goes through several shape changes and departs as a cylindrical bubble. The departing bubble creates a wall jet that impinges on the lower interface of the bubble and forms a dimple. Thereafter, the vapor mass tries to acquire a spherical shape as it moves away from the wall. The rapid acceleration of the vapor mass breaks down the merger process before the cycle repeats itself. The bubble shapes, as well as the merger behavior predicted from the numerical simulations, is in very good agreement with the visual observations.

3.2.2 Lateral Bubble Merger and Formation of Mushroom Type Bubbles. As the wall superheat is increased, the number density of the active nucleation sites also increases; consequently, vapor bubbles nucleating at adjacent sites begin to merge laterally. Mukherjee and Dhir [47] have carried out numerical simulations and experiments for merger of two bubbles nucleating at adjacent sites. In Fig. 14 the upper set of frames show the results of visual observations, whereas the results of numerical simulations are depicted in the lower set of frames. Once the two bubbles merge laterally, a mushroom shaped bubble with two stems attached to the heater surface is formed. Note the existence of a liquid bridge between the two stems. As the merged vapor mass tries to acquire a spherical shape as a result of surface tension, vapor tails are formed. The vapor bubble then oscillates both in the plane of the photographs and normal to it before detaching. Numerical simulations capture the essential physics of the process—formation of vapor tails and bubble oscillations prior to departure. However, the extent of trapped liquid in numerical simulations is less than that seen in the experiments.

A quantitative comparison of the predictions from numerical simulations of the growth history of the two bubble merger case with data from experiments is made in Fig. 15. Bubble equivalent diameter in Fig. 15 is the diameter of a perfect sphere having the

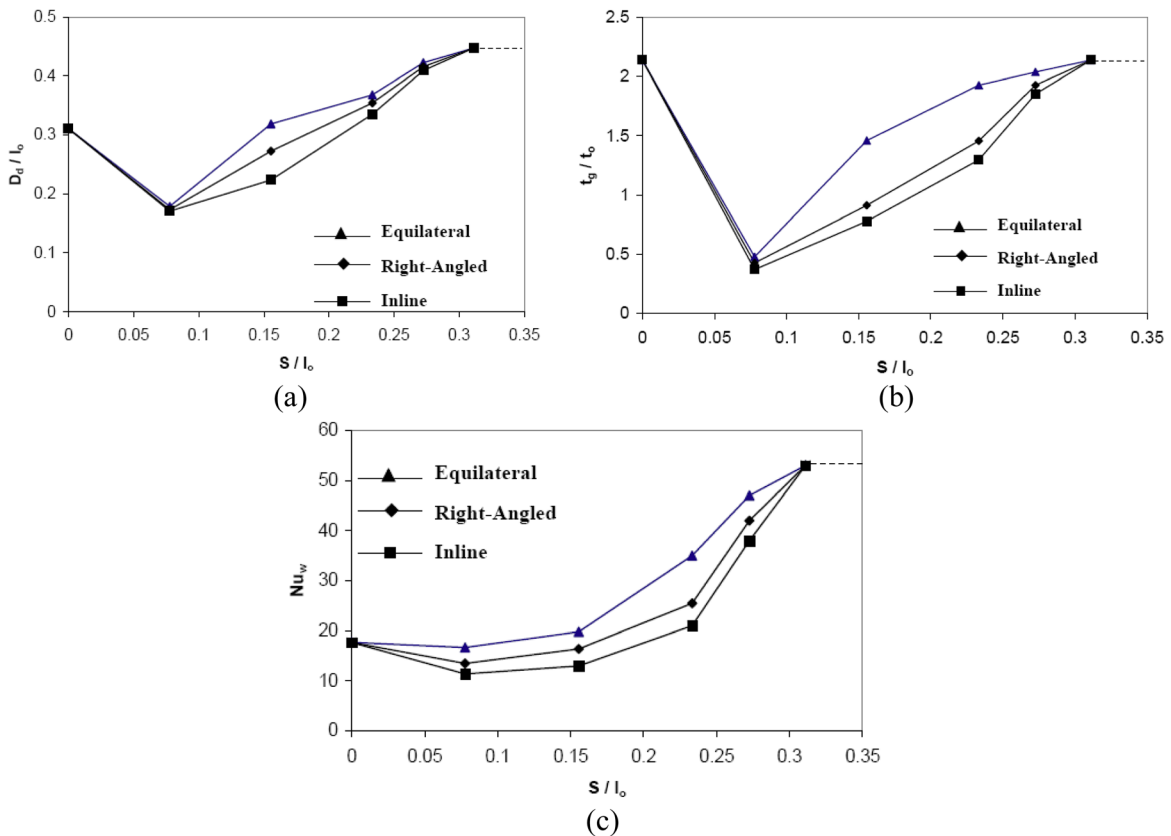


Fig. 17 Effect of spacing (a) dimensionless bubble departure diameter, (b) dimensionless growth time, and (c) Nusselt number (fluid: sat. PF5060, $\Delta T_w = 10^\circ\text{C}$, $\varphi = 10$ deg, $g/g_e = 10^{-2}$, from [48])

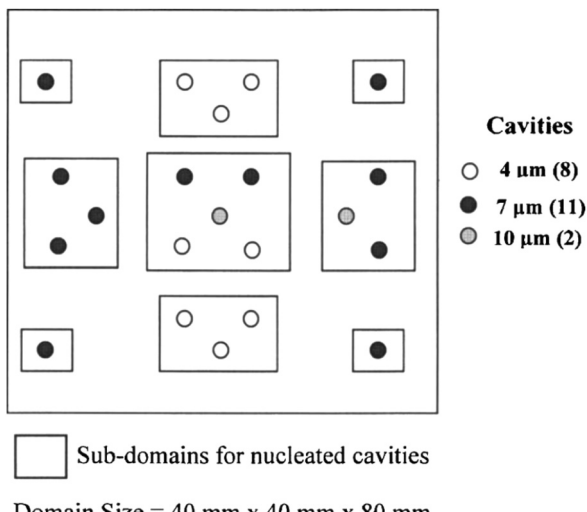


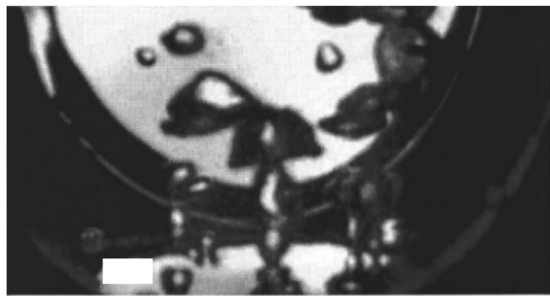
Fig. 18 Simulated commercial surface (from [48])

same volume as the volume of two single bubbles or the merged vapor mass. Numerical simulation results, shown by the solid line, appear to describe well not only the growth history, but also the bubble departure diameter and the growth period.

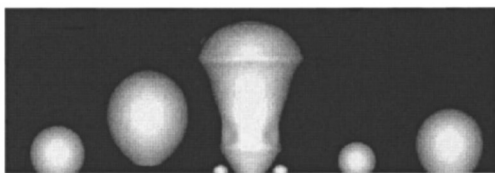
Merger of multiple bubble (inline and in a plane) has been systematically investigated [40,48]. In these simulations, parameters such as cavity spacing, cavity arrangement, gravity level, and contact angle were varied. In general, numerical simulations show that the predicted vapor bubble departure diameter after merger is smaller than that of a single bubble. Figure 16(a) shows a comparison of predicted growth histories of merger of three inline bub-

bles and that of a single bubble; Fig. 16(b) shows the net forces on the bubbles. Equivalent bubble departure diameter and the corresponding growth period for the three bubble merger case are smaller than those of the single bubble. In order to determine the cause of the premature departure of vapor mass after merger, the net force acting on the vapor mass was calculated; this force is taken to be positive when acting upwards and negative when acting downwards. For the three bubble merger case, the force changes sign from negative to positive at about 7 ms. This is about the time when the bubble base (Fig. 16(a)) starts to shrink after reaching its maximum value and the vapor bubble enters the detachment phase. However, the single bubble continues to experience negative force and steadily grows for a substantial period of time beyond which the merged vapor mass starts to detach. The difference between the force acting on the merged vapor mass and the single bubble when the vapor mass, after merger, starts to detach is termed as "lift force." This force is responsible for the premature departure of the vapor mass after merger. The importance of this force increases as the level of gravity decreases.

Figure 17 shows numerical predictions of equivalent bubble diameter at departure, growth period, and time averaged Nusselt number at the wall as a function of cavity spacing during the merger of three bubbles. Three different orientations were simulated: (i) inline, (ii) right-angle triangle, and (iii) equilateral triangle. These calculations were carried out for saturated PF5060 using a domain of 7.34 mm x 7.34 mm x 14.68 mm; $\Delta T_w = 10^\circ\text{C}$, $\varphi = 10$ deg, $g/g_e = 10^{-2}$. The equivalent bubble diameters at departure and cavity spacing are normalized using the characteristic length (l_o , Eq. (20)); the growth period is normalized using the characteristic time scale ($t_o = \sqrt{l_o/g}$). From Fig. 17(a) it can be seen that, irrespective of the cavity orientation, bubble departure diameter decreases as the spacing between cavities increases until the spacing is equal to $D_{ds}/4$, where D_{ds} is the departure diameter of a single bubble. Thereafter, the departure diameter increases

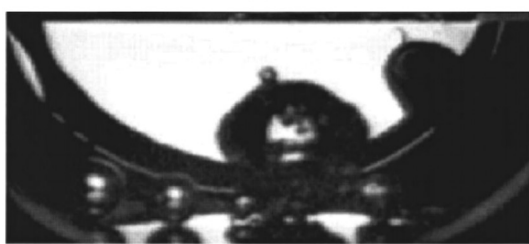


Experiments of Qiu et al.

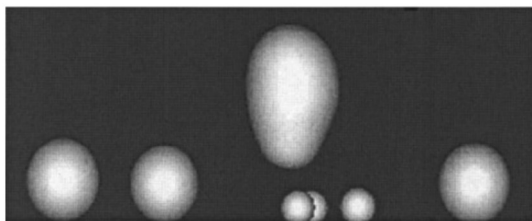


Numerical simulation

(a)



Experiments of Qiu et al.



Numerical simulation

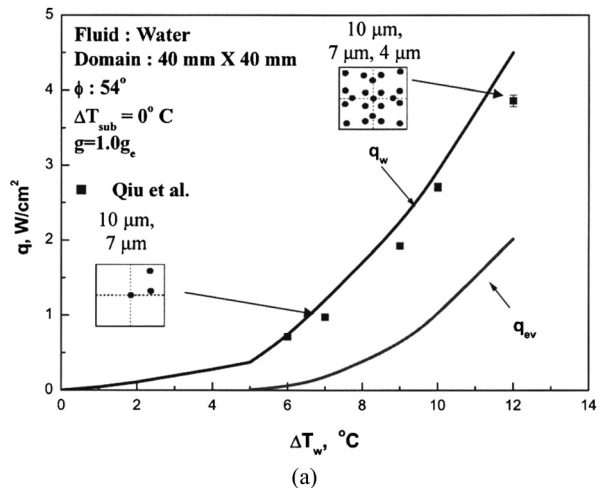
(b)

Fig. 19 Comparison of experimental and predicted bubble shapes during nucleate boiling on a simulated commercial surface (a) $g/g_e=1$ and (b) $g/g_e=10^{-2}$ (fluid: sat. water, $\Delta T_w=7^\circ\text{C}$, from [48])

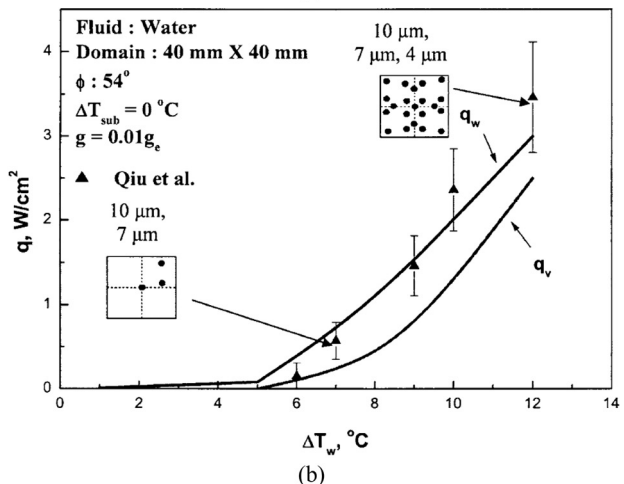
until the spacing is large enough so that bubbles do not merge. For a given spacing, the bubble departure diameter increases from inline to right angle to equilateral triangle orientations. The limiting value of departure diameter is equal to that of single bubble when spacing between cavities is zero, and is equal to $\sqrt{3}D_{ds}$ when the spacing is $1.4l_o$. The growth period was found to show a behavior similar to the bubble diameter at departure. It should be noted that depending on the spacing between cavities, bubble departure diameter can vary by a factor of 2 and the growth period by a factor of 3. Similar behavior was noted at other gravity levels.

4 Nucleate Boiling

Very few numerical simulations have been carried out to predict nucleate boiling heat flux as a function of wall superheat. Abarajith [48] used numerical simulations to predict the heat flux on a surface simulating a commercial surface. On this polished silicon wafer surface, $4\text{ cm} \times 4\text{ cm}$ in area, cylindrical cavities of 10, 7, and $4\text{ }\mu\text{m}$ in diameter were fabricated as shown in Fig. 18. Dif-



(a)



(b)

Fig. 20 The variation of wall heat flux with wall superheat for saturated water (a) $g/g_e=1$ and (b) $g/g_e=10^{-2}$ (from [48])

ferent size cavities were chosen so that smaller cavities become active as wall superheat is increased in a manner similar to that for a commercial surface. In order to accelerate the computations on a large domain, subdomains as depicted in Fig. 18 were defined around clusters of cavities. While carrying out the computations, no interactions were allowed between neighboring domains. Heat flux in the regions falling between the domains was obtained by interpolating across the values that exist at the boundaries of the domains. The effect of gravity level on the variation of the nucleate boiling heat flux was also investigated.

The top portion of Fig. 19(a) shows the visual observation of the boiling phenomenon on the above described surface when 6–7 cavities were active at earth normal gravity ($g/g_e = 1$). The lower figure shows the results of computations at one instant of time. Figure 19(b) shows a similar comparison when the gravity level is reduced by a factor of 100 ($g/g_e = 10^{-2}$). The experiments investigation were carried out by Qiu et al. [38] using the same heater surface at Earth's gravity and during parabolic flights onboard the KC-135 aircraft. Observed and predicted vapor removal configurations in both situations are in a qualitative agreement.

Figure 20 shows a comparison of wall heat flux as a function of wall superheat predicted from numerical simulations with data from experiments [38] for $g/g_e = 1$ and 10^{-2} . The solid line is the prediction from numerical simulations when the number of cavities that are active and their location is given as an input to the simulations. The reported results are post several bubble growth and departure cycles. At both gravity levels, the predictions compare reasonably well with the data, though larger scatter is observed in the low-gravity experimental data due to the

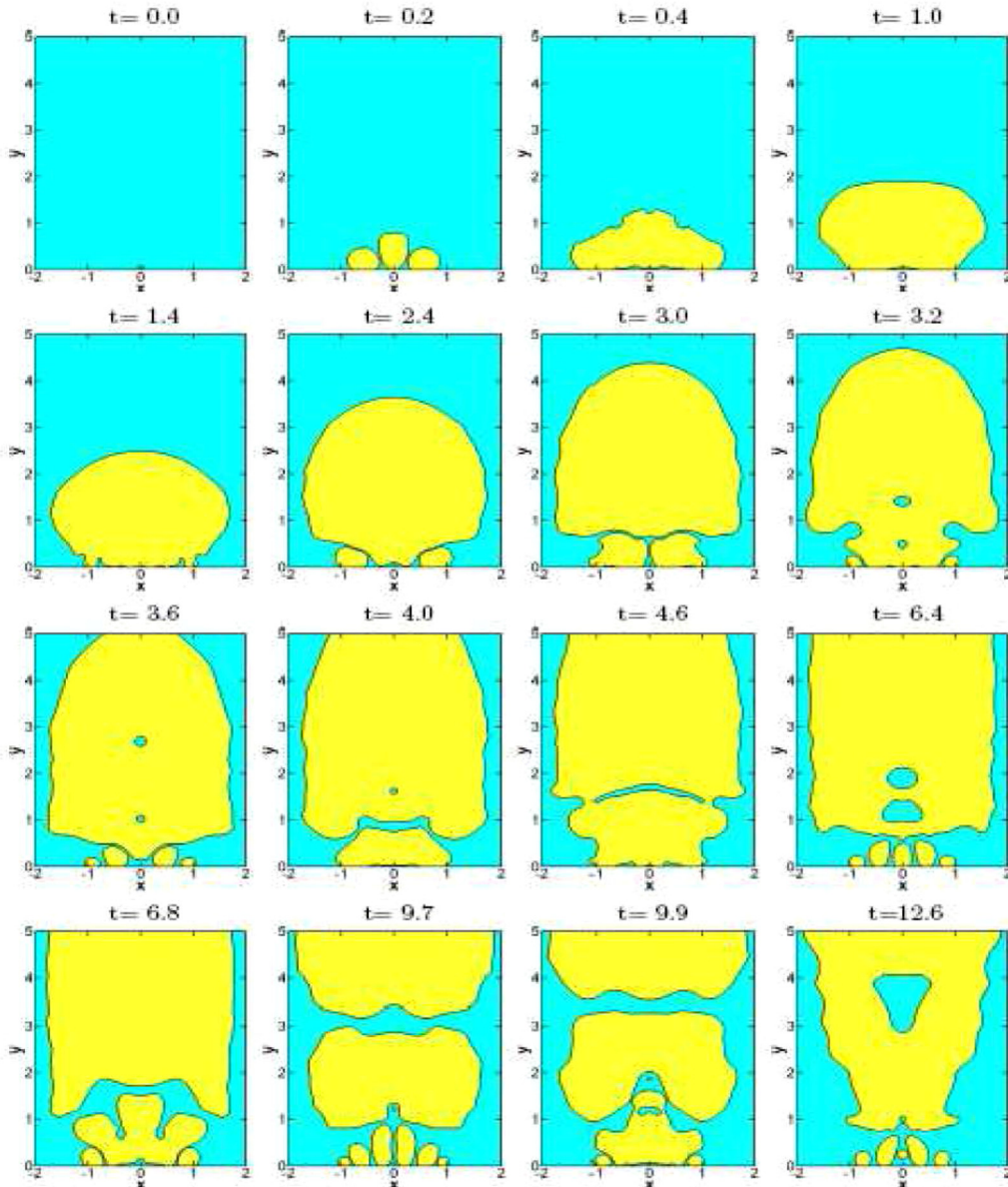


Fig. 21 Bubble growth and merger for $\Delta T_w = 25^\circ\text{C}$ (from [49])

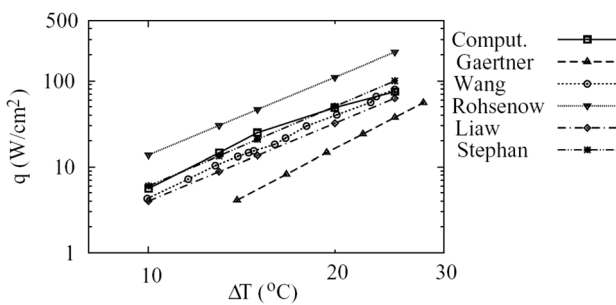


Fig. 22 Comparison of the numerical results with experimental data and correlations (from [49])

uncertainty in the calculation of the heat loss. The lower curves in Figs. 20(a) and 20(b) represent the wall energy that goes into production of vapor. Comparison of the two nucleate boiling curves shows that the heat fluxes obtained in low-gravity conditions are lower than those obtained at earth normal gravity; at the highest wall superheat it is almost 25% lower. Although the fraction of

wall energy utilized in production of vapor varies with wall superheat, at a wall superheat of 12°C , almost 40% of the energy is utilized for vapor production at $g/g_e = 1$. In comparison, at $g/g_e = 10^{-2}$, approximately 80% of energy is predicted to be consumed in vapor production. The remaining energy goes into superheating of liquid.

Son and Dhir [49] have investigated multiple bubble merger during saturated nucleate boiling. In these two-dimensional (2D) simulations, the wall superheat was specified. Both the active nucleation site density [50] and the bubble waiting time [1,2] were specified as a function of wall superheat. Figure 21 shows the bubble growth and merger process for a wall superheat of 20°C . Numerical results show that at low wall superheats, discrete bubbles are released from the heater and bubble merger occurs only occasionally. With increase in wall superheat, bubble merger in both the vertical and lateral direction occur frequently, leading to the formation of large vapor columns or mushroom-type bubbles. Figure 22 shows a comparison of the predicted nucleate boiling curve (2D) with correlations available in the literature. The heat fluxes obtained from the present 2D analysis are within $\pm 25\%$ with those predicted from Stephan and Abdelsalam's [51]

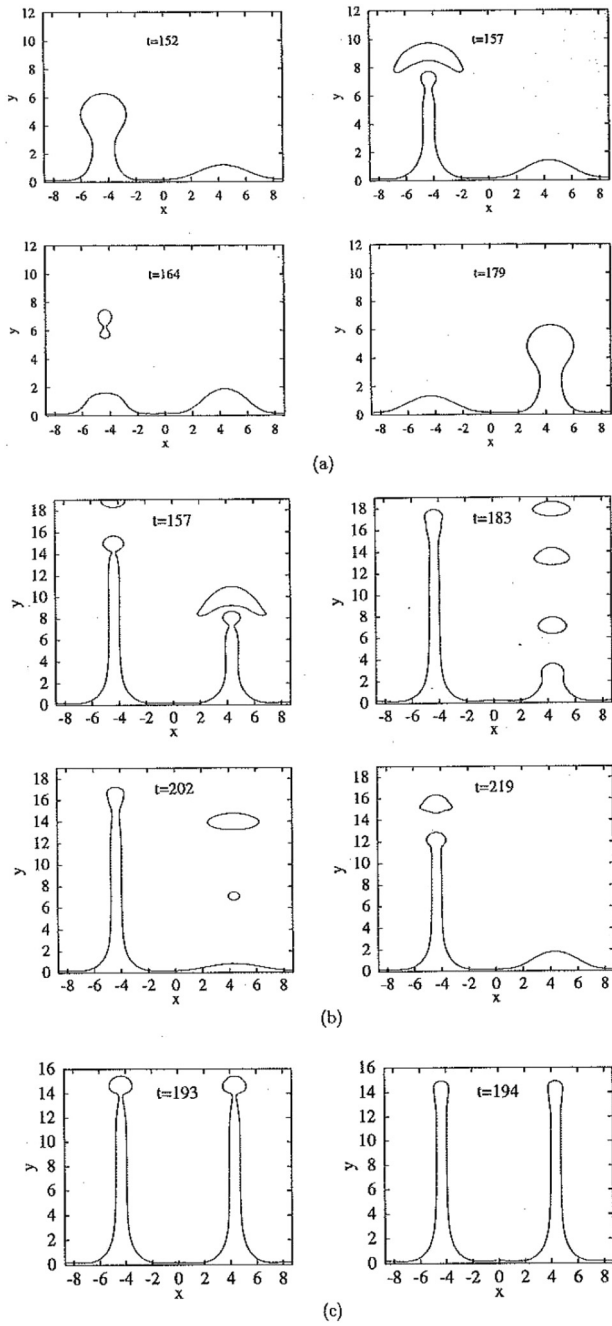


Fig. 23 Evolution of liquid-vapor interface at near critical pressures (a) $\Delta T_w = 10^\circ\text{C}$, (b) $\Delta T_w = 22^\circ\text{C}$, and (c) $\Delta T_w = 30^\circ\text{C}$ (from [6])

correlation. In nucleate boiling, the steep variation of heat flux with wall superheat is caused not only by the increase in the number density of active sites with wall superheat but also by the reduction in the growth and waiting periods. Additional three-dimensional (3D) simulations were also performed using a very coarse grid, due to excessive computational time. Results of the 3D simulation were found to be about 40% lower than that obtained for the corresponding 2D case. The numerical simulations were carried out only up to 80% of the critical heat flux.

5 Film Boiling

The first numerical simulation of film boiling was performed by Son and Dhir [52], wherein saturated film boiling on a horizontal surface was studied. The simulations were performed in axisym-

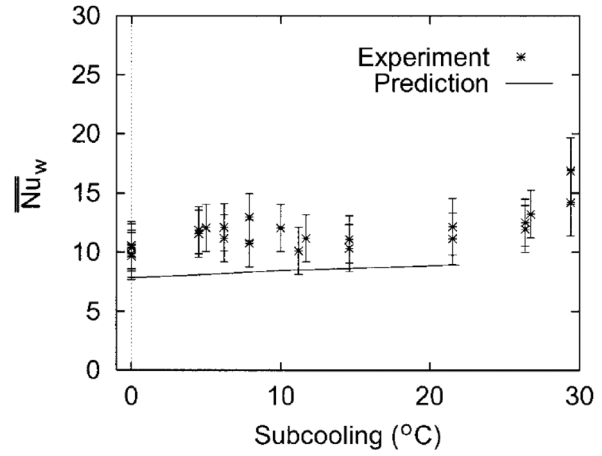


Fig. 24 Comparison of predicted area-averaged wall Nusselt number with experimental data, for $\Delta T_w = 100^\circ\text{C}$ and $\Delta T_{\text{sub}} = 0$ to 22°C (from [57,58])

metric two-dimensional curvilinear coordinates. A moving mesh was used to capture the liquid-vapor interface and the wall temperature was maintained constant. The surface tension was modeled as a volumetric source term [53] in the momentum equation. The conservation equations were solved in both the liquid and vapor phases to determine the temperature and flow fields. Soon thereafter, Son and Dhir [6] incorporated the level set method into their previous numerical model. This allowed the simulation to capture the breaking and merging of the interface effectively. Film boiling of saturated water on a horizontal surface at near critical pressures was also investigated in this study. Figure 23 shows the evolution of the interface at a reduced pressure (P/P_c) of 0.99 ($T_{\text{sat}} = 373.3^\circ\text{C}$) for $\Delta T_w = 10$ and 22°C . The numerical results show that at low wall superheats, discrete bubbles are released alternatively at the nodes and antinodes. On the other hand, vapor jets are formed at both the nodes and antinodes as the wall superheat is increased. This behavior was found to be consistent with visual observations reported in the literature. The area- and time-averaged Nusselt number was found to be bounded by the predictions of Berenson [54] and Klimenko [55].

Juric and Tryggvason [56] used the so-called phase-field formulation to investigate film boiling on a horizontal surface. A two-dimensional Cartesian coordinate system was used for these simulations. The liquid-vapor interface was captured using a front-tracking method. A constant wall heat flux boundary condition was imposed on the bottom wall. Numerical results of the wall heat flux and wall temperature distribution were found to be in good agreement with experimental data.

Banerjee and Dhir [57,58] performed a three-dimensional Taylor instability analysis during subcooled film boiling on a horizontal disk. They found that the most dominant Taylor wavelength was the same as that obtained from a two-dimensional analysis in Cartesian coordinates. Increase in liquid subcooling resulted in the decrease in the vapor film thickness, and an increase in the area- and time-averaged Nusselt number. A comparison of the numerically predicted time- and area-averaged Nusselt number and the experimental data is shown in Fig. 24 for $\Delta T_w = 10^\circ\text{C}$ and varying liquid subcooling (0 to 22°C).

Welch and Wilson [59] adopted a volume-of-fluid (VOF) method to simulate film boiling on a horizontal surface for constant wall superheat conditions. Their numerical results showed the quasi-steady periodic bubble release pattern obtained in the earlier study of Son and Dhir [52]. Welch and Rachidi [60] modified the model of Welch and Wilson [59] to include a solid wall. Constant heat flux was applied at the lower solid boundary. The results obtained for Nusselt numbers are in reasonable agreement with existing correlations. The authors found that

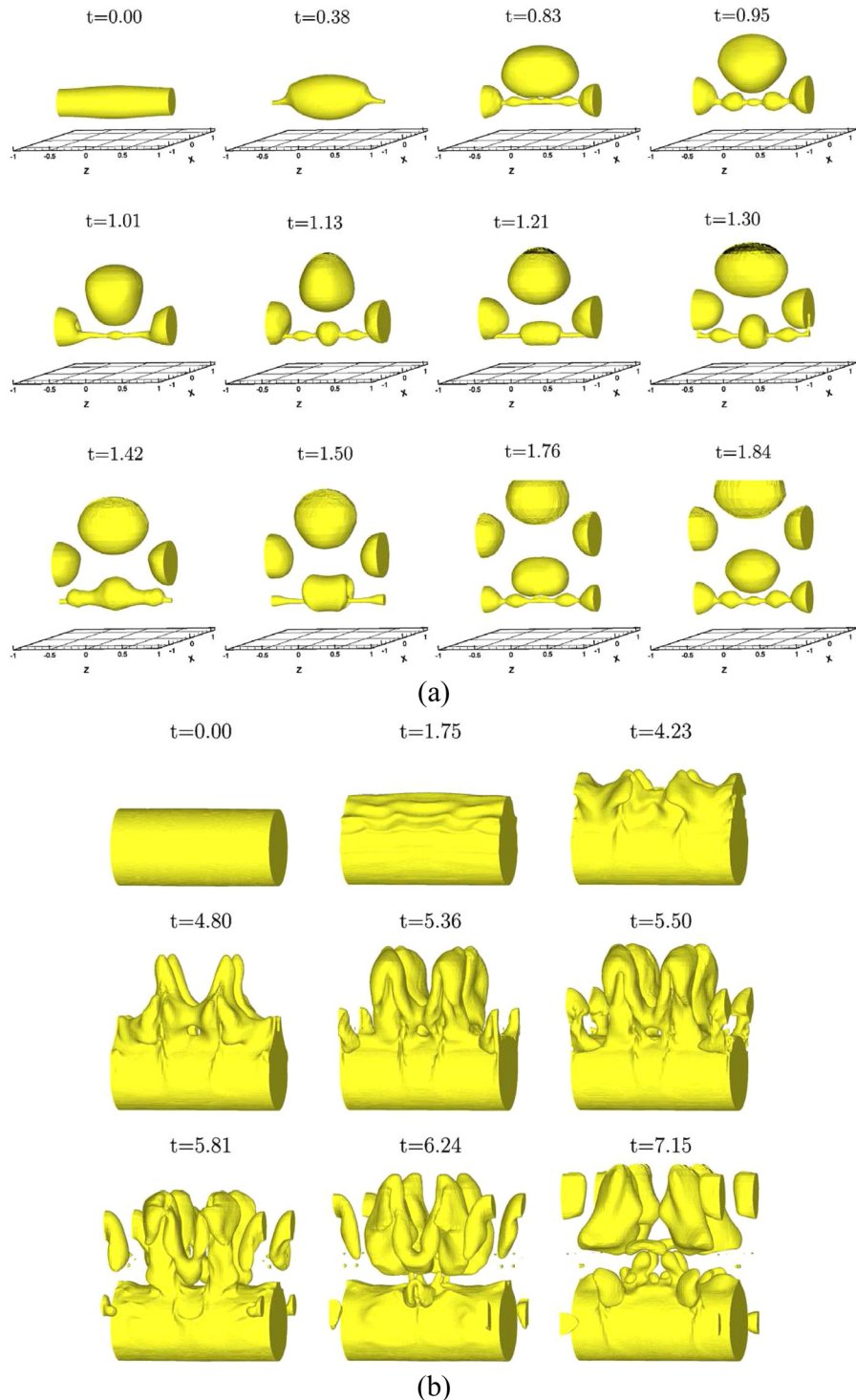


Fig. 25 Evolution of liquid-vapor interface at $g/g_e = 1$ (a) $D = 0.125\text{ mm}$ and (b) $D = 12.5\text{ mm}$ (from [7])

the presence of the wall results in surface temperature fluctuations of about 1 K, at a wall temperature of approximately 650 K. They concluded that the solid wall acted as a heat source or sink and helped attenuate the temperature fluctuations of the wall.

Other notable numerical simulations of film boiling on horizontal surfaces were those by Esmaeeli and Tryggvason [8], Tomar et al. [9], and Agarwal et al. [10]. Welch and Biswas [11] and later Tomar et al. [12] investigated the effect of an applied electric field on film boiling heat transfer. In these studies, the conservation equation for the electric field was also solved and an additional

volumetric electrohydrodynamic force was incorporated into the momentum equation. Numerical results showed that when an electric field was applied, the bubble separation distance decreased, the instabilities grow faster, and as a result bubble release frequency increased. The Nusselt number also increased with increase in the electric field.

More recently, Son and Dhir [7] simulated saturated film boiling on a horizontal cylinder by using an immersed solid boundary to represent the cylindrical solid heater in a pool of liquid. A constant wall superheat condition was used in these simulations. The

effect of cylinder diameter (D) and gravity level (g/g_e) was studied. Figure 25 shows the evolution of the liquid-vapor interface for saturated film boiling on horizontal cylinders for two different cylinder diameters. Simulation results show that for small diameter cylinders (Fig. 25(a)), discrete bubbles are released cyclically from the top portion of the cylinder. On the other hand, for large cylinders (Fig. 25(b)), the bubbles are released at various circumferential locations in a two-dimensional wave pattern. This bubble release pattern has been found to be consistent with those seen in experiments. The numerical results were found to be within $\pm 10\%$ of those predicted from Sakurai et al.'s [61] correlation.

6 Future Work

6.1 Conjugate Heat Transfer. In heat flux controlled situations, the thermal response of the heater (in 3D) should be an integral part of any future simulation effort because the bubble dynamics is dependent on both the thermal response of the heater and the heat transfer occurring on the fluid side. Another deficiency in the simulations that do not include the thermal response of the heater is that the bubble waiting time needs to be specified. In simulations performed to date, the bubble waiting time was specified a priori, based on empirical correlations [1] and/or visual observation during experiments. Inclusion of a model for the solid in the simulations eliminates the need to specify the bubble waiting time explicitly. The waiting time is implicitly calculated as part of the thermal response of the solid, provided a criterion for bubble nucleation, such as wall superheat required for nucleation for a given cavity size, is specified.

6.2 Extend Modeling Effort to Commercial Surfaces. Once the thermal response of the heater is included in the simulations, the bubble waiting time does not have to be specified explicitly. This approach can then be extended to simulations of a commercial surface, provided information regarding cavity size and distribution on the surface is known. Hence, once the material of the heater is selected, the number of cavities present on the surface combined with a criterion such as the one developed by Wang and Dhir [45] can be used to determine the number of active cavities at a particular wall superheat. Alternately, one could use correlations such as the one developed by Basu et al. [50] to determine the active nucleation site density as a function of wall superheat. The cavities or defects on a commercial surface are randomly distributed. Sensitivity analysis can be performed to ascertain the effect of cavity distribution on the predicted wall heat flux. Once results of such numerical simulations are validated with experimental data, it will be possible, in the near future, to predict the complete boiling curve prior to experiments. This will be particularly valuable for those applications where conducting experiments is difficult, time consuming, and very expensive (e.g., space related applications, nuclear reactors, boilers, etc.). It is also expected that numerical simulations will shed light on the effect of contact angle on critical heat flux and on the limitations imposed by hydrodynamics versus thermal limitation at the surface.

6.3 Parallel Computations. Of the various modes of boiling, nucleate and transition boiling regimes are the most challenging. As such most of our efforts need to be focused on these boiling regimes. All previous attempts to perform full three-dimensional simulations of nucleate boiling have been limited primarily due to the enormous computing power required and the corresponding memory requirements. For example, for realistic nucleate boiling simulations on a commercial surface, the heater size has to be at least $2.5 \text{ cm} \times 2.5 \text{ cm}$ (for water at normal gravity, most dangerous Taylor wavelength, $\lambda_d \approx 2.5 \text{ cm}$). At a wall superheat of 20°C , the predicted active nucleation site density is 96 sites/cm^2 [50] or total active sites ≈ 600 , on the surface. Based on past experience,

accurately simulation of the bubble dynamics will require a minimum of 100 grids/ l_o in each dimension (for water at atmospheric pressure and earth normal gravity, $l_o \approx 2.5 \text{ mm}$); for a domain 2.5 cm in height, this translates to about 10^9 total grid points. Even if sufficient computer memory is available, a problem of this magnitude cannot be solved in any reasonable amount of time using serial computations. As such, the only option is to use parallel computations.

6.4 Experimental Data. Future experimental work should involve measurement of the thermal response of the solid during bubble growth and departure on microfabricated surfaces. Detailed experiments with single and multiple bubbles with different heater material should be conducted. Such experiments will provide valuable data for validation of numerical simulations at different levels.

7 Summary

Over the last decade or so significant progress has been made to numerically simulate nucleate and film boiling under pool conditions. In this paper a review of the results of numerical simulations and their validation with experimental data has been presented. For nucleate boiling, single bubble dynamics, bubble merger, and influence of noncondensables has been investigated for different wall superheats, liquid subcoolings, contact angles, and magnitudes of level of gravity. Limited work has also been reported while solving conjugate heat transfer in the solid, when heat flux instead of wall temperature condition is imposed. Functional dependence of nucleate boiling heat flux on wall superheat has also been studied by either using microfabricated surfaces on which the number of active cavities is known or using correlations available in the literature. Similarly for a specific wall superheat, correlations have to be used to specify the waiting period. Future effort for prediction of nucleate and transition boiling heat flux should simultaneously involve solution of conjugate heat transfer in the solid. It will also require significantly enhanced computational capacity.

Film boiling simulations have been performed primarily for horizontal surfaces. Modeling of transition from nucleate to film boiling and film to nucleate boiling needs further work before one can numerically predict the complete pool boiling curve, at least for a horizontal surface.

Nomenclature

A	= dispersion constant
C_g	= mass fraction of noncondensable ($= \rho_g / \rho_m$)
c_p	= specific heat capacity at constant pressure (J/kg K)
D	= diffusion coefficient (m^2/s)
\vec{g}	= gravity vector (m/s^2)
g_e	= Earth's normal gravity (m/s^2)
H	= Heaviside step function
h	= grid spacing for macro region
h_{ev}	= evaporative heat transfer coefficient ($\text{W/m}^2 \text{ K}$)
h_{fg}	= latent heat of vaporization (J/kg)
k	= thermal conductivity (W/m K)
L	= width of computational domain (m)
l_o	= characteristic length scale (m)
M	= molecular weight (g/mol)
p	= pressure (Pa)
q	= heat flux (W/m^2)
R	= radius of computational domain or bubble (m)
R_o	= radius of dry region beneath a bubble (m)
R_1	= radial location of the interface at $y = h/2$ (m)
\bar{R}	= universal gas constant (J/mol K)
r	= radial coordinate (m)
T	= temperature ($^\circ\text{C}$ or K)
t	= time (s)
t_o	= characteristic time scale (s)

- ΔT = temperature difference ($^{\circ}\text{C}$ or K)
 \vec{u} = velocity vector (m/s)
 u_o = characteristic velocity scale (m/s)
 \dot{V}_{micro} = rate of vapor volume production from the microlayer (m 3 /s)
 $\Delta \dot{V}_{\text{micro}}$ = vapor-side control volume (m 3)
 x = volume fraction
 Y = height of computational domain (m)
 y = vertical coordinate (m)

Greek Symbols

- δ = liquid film thickness (m)
 δ_o = nonevaporating liquid film thickness (m)
 δ_t = thermal boundary layer thickness (m)
 ϕ = level-set function
 φ = contact angle (deg)
 κ = interfacial curvature (1/m)
 λ = wavelength (m)
 μ = dynamic viscosity (Pa s)
 ρ = density (kg/m 3)
 σ = surface tension (n/m)

Subscripts

- 0 = initial condition
 o = reference value
 d = most dangerous
 g = gas
 int = interface
 l = liquid
 m = mixture inside bubble
 sat = saturation
 sub = subcooling
 v = vapor
 w = wall

Superscripts

- $'$ = radial derivative ($=\partial/\partial r$)
 T = transpose

References

- [1] Basu, N., Warrier, G. R., and Dhir, V. K., 2005, "Wall Heat Flux Partitioning During Subcooled Flow Boiling: Part I—Model Development," *ASME J. Heat Transfer*, **127**(2), pp. 131–140.
- [2] Basu, N., Warrier, G. R., and Dhir, V. K., 2005, "Wall Heat Flux Partitioning During Subcooled Flow Boiling: Part II—Model Validation," *ASME J. Heat Transfer*, **127**(2), pp. 141–148.
- [3] Warrier, G. R., and Dhir, V. K., 2006, "Heat Transfer and Wall Heat Flux Partitioning During Subcooled Flow Nucleate Boiling—A Review," *ASME J. Heat Transfer*, **128**(12), pp. 1243–1256.
- [4] Dhir, V. K., 2006, "Mechanistic Prediction of Nucleate Boiling Heat Transfer—Achievable or a Hopeless Task?," *ASME J. Heat Transfer*, **128**(1), pp. 1–12.
- [5] Kalinin, E. K., Berlin, I. I., and Kostyuk, V. V., 1975, "Film-Boiling Heat Transfer," *Adv. Heat Transfer*, **11**, pp. 51–197.
- [6] Son, G., and Dhir, V. K., 1998, "Numerical Simulation of Film Boiling Near Critical Pressure With Level Set Method," *ASME J. Heat Transfer*, **120**(1), pp. 183–192.
- [7] Son, G., and Dhir, V. K., 2008, "Three-Dimensional Simulation of Saturated Film Boiling on a Horizontal Cylinder," *Int. J. Heat Mass Transfer*, **51**, pp. 1156–1167.
- [8] Esmaeeli, A., and Tryggvason, G., 2004, "Computations of Film Boiling. Part I: Numerical Method," *Int. J. Heat Mass Transfer*, **47**, pp. 5451–5461.
- [9] Tomar, G., Biswas, G., Sharma, A., and Agrawal, A., 2005, "Numerical Simulation of Bubble Growth in Film Boiling Using a Coupled Level-Set and Volume-of-Fluid Method," *Phys. Fluids*, **17**, p. 112103.
- [10] Agarwal, D. K., Welch, S. W. J., Biswas, G., Durst, F., 2004, "Planar Simulation of Bubble Growth in Film Boiling in Near-Critical Water Using a Variant of the VOF Method," *ASME J. Heat Transfer*, **126**(3), pp. 329–338.
- [11] Welch, S. W., and Biswas, G., 2007, "Direct Simulation of Film Boiling Including Electrohydrodynamic Forces," *Phys. Fluids*, **19**, p. 012106.
- [12] Tomar, G., Biswas, G., Sharma, A., and Welch, S. W. J., 2009, "Influence of Electric Field on Saturated Film Boiling," *Phys. Fluids*, **21**, p. 032107.
- [13] Witte, L. C., and Lienhard, J. H., 1982, "On the Existence of Two Transition Boiling Curves," *Int. J. Heat Mass Transfer*, **25**, pp. 771–779.
- [14] Bui, T. D., and Dhir, V. K., 1985, "Transition Boiling Heat Transfer on a Vertical Surface," *ASME J. Heat Transfer*, **107**(4), pp. 756–763.
- [15] Liaw, S. P., and Dhir, V. K., 1986, "Effect of Surface Wettability on Transition Boiling Heat Transfer From a Vertical Surface," Proceedings of 8th International Heat Transfer Conference, San Francisco, CA, Vol. 4, pp. 2031–2038.
- [16] Auracher, H., and Marquardt, W., 2002, "Experimental Studies of Boiling Mechanisms in All Boiling Regimes Under Steady-State and Transient Conditions," *Int. J. Thermal Sci.*, **41**, pp. 586–598.
- [17] Lee, R. C., and Nyadhl, J. E., 1989, "Numerical Calculation of Bubble Growth in Nucleate Boiling From Inception to Departure," *ASME J. Heat Transfer*, **111**(2), pp. 474–479.
- [18] Cooper, M. G., and Lloyd, A. J. P., 1969, "The Microlayer in Nucleate Boiling," *Int. J. Heat Mass Transfer*, **12**, pp. 895–913.
- [19] Mei, R., Chen, W., and Klausner, J. F., 1995, "Vapor Bubble Growth in Energetic Boiling—I. Growth Rate and Thermal Fields," *Int. J. Heat Mass Transfer*, **38**, pp. 921–934.
- [20] Welch, S. W. J., 1998, "Direct Simulation of Vapor Bubble Growth," *Int. J. Heat Mass Transfer*, **41**, pp. 1655–1666.
- [21] Son, G., Dhir, V. K., and Ramanujapu, N., 1999, "Dynamics and Heat Transfer Associated With a Single Bubble During Nucleate Boiling on a Horizontal Surface," *ASME J. Heat Transfer*, **121**(3), pp. 623–632.
- [22] Sussman, M., Smereka, P., and Osher, S., 1994, "A Level Set Approach for Computing Solutions to Incompressible Two-Phase Flow," *J. Comput. Phys.*, **114**, pp. 146–159.
- [23] Wayner, P. C., Jr., 1992, "Evaporation and Stress in the Contact Line Region," Proceedings of the Engineering Foundation Conference on Pool and External Flow Boiling, Santa Barbara, CA, pp. 251–256.
- [24] Wayner, P. C., Jr., 1999, "Intermolecular Forces in Phase-Change Heat Transfer: 1998 Kern Award Review," *AICHE J.*, **45**, pp. 2055–2068.
- [25] Maroo, S. C., and Chung, J. N., 2009, "Nanoscale Liquid-Vapor Phase-Change Physics in Nonevaporating Region at the Three-Phase Contact Line," *J. Appl. Phys.*, **106**, p. 064911.
- [26] Stephan, P., and Hammer, J., 1994, "A New Model for Nucleate Boiling Heat Transfer," *Wärme. Stoffübertragung*, **30**, pp. 119–125.
- [27] Lay, J. H., and Dhir, V. K., 1995, "Shape of Vapor Stem During Nucleate Boiling of Saturated Liquids," *ASME J. Heat Transfer*, **117**(2), pp. 394–401.
- [28] Ramanujapu, N., and Dhir, V. K., 1999, "Dynamics of Contact Angle During Growth and Detachment of a Vapor Bubble at a Single Nucleation Site," Proceedings of the 5th ASME/JSME Joint Thermal Engineering Conference, San Diego, CA, ASME, New York.
- [29] Singh, S., and Dhir, V. K., 2000, "Effect of Gravity, Wall Superheat and Liquid Subcooling on Bubble Dynamics During Nucleate Boiling," *Microgravity Fluid Physics and Heat Transfer*, V. K. Dhir, ed., Begell House, New York, pp. 106–113.
- [30] Abarajith, H. S., and Dhir, V. K., 2002, "Effect of Contact Angle on the Dynamics of a Single Bubble During Pool Boiling Using Numerical Simulations," Proceedings of IMECE2002 ASME International Mechanical Engineering Congress & Exposition, New Orleans, LA, Paper IMECE2002-33876, pp. 467–475.
- [31] Fritz, W., 1935, "Maximum Volume of Vapor Bubbles," *Phys. Z.*, **36**, pp. 379–384.
- [32] Nam, Y., Aktinol, A., Dhir, V. K., and Ju, Y. S., 2011, "Single Bubble Dynamics on a Superhydrophilic Surface With Artificial Sites," *Int. J. Heat Mass Transfer*, **54**, pp. 1572–1577.
- [33] Wu, J., and Dhir, V. K., 2011, "Numerical Simulation of Dynamics and Heat Transfer Associated With a Single Bubble in Subcooled Boiling and in the Presence of Noncondensables," *ASME J. Heat Transfer*, **133**(4), p. 041502.
- [34] Wu, J., Dhir, V. K., and Qian, J., 2007, "Numerical Simulation of Subcooled Nucleate Boiling by Coupling Level Set Method With Moving Mesh Method," *Numer. Heat Transfer Part B*, **51**, pp. 535–563.
- [35] Siegel, R., and Keshock, E. G., 1964, "Effects of Reduced Gravity on Nucleate Boiling Bubble Dynamics in Saturated Water," *AICHE J.*, **10**, pp. 509–517.
- [36] Straub, J., 2001, "Boiling Heat Transfer and Bubble Dynamics in Microgravity," *Adv. Heat Transfer*, **35**, pp. 58–172.
- [37] Merte, H., Lee, H. S., and Keller, R. B., 1995, "Report on Pool Boiling Experiment Flow on STS-47, STS-57, STS-60," Report No. UM-MEAM-95-01.
- [38] Qiu, D. M., Dhir, V. K., Hasan, M. M., and Chao, D., 2000, "Single and Multiple Bubble Dynamics During Nucleate Boiling Under Low Gravity Conditions," Proceedings of the National Heat Transfer Conference, Pittsburgh, PA.
- [39] Dhir, V. K., Warrier, G. R., Aktinol, E., Chao, D., Eggers, J., Sheredy, W., and Booth, W., 2011, "Nucleate Pool Boiling Experiments (NPBX) on the International Space Station," *Microgravity Sci. Technol.*, **24**, pp. 307–325.
- [40] Abarajith, H. S., Dhir, V. K., and Son, G., 2004, "Numerical Simulation of the Dynamics of Multiple Bubble Merger During Pool Boiling Under Reduced Gravity Conditions," Proceedings of 7th Japan-U.S. Seminar on Two-Phase Flow Dynamics, Moriyama, Japan.
- [41] Zhao, J. F., Li, Z. D., and Zhang, L., 2011, "Numerical Simulation of Single Bubble Pool Boiling in Different Gravity Conditions," *AIP Conf. Proc.*, **1376**, pp. 565–568.
- [42] Kunkelmann, C., and Stephan, P., 2009, "CFD Simulation of Boiling Flows Using the Volume-of-Fluid Method Within OPENFOAM," *Numer. Heat Transfer Part A*, **56**, pp. 631–646.
- [43] Kunkelmann, C., and Stephan, P., 2010, "Numerical Simulation of the Transient Heat Transfer During Nucleate Boiling of Refrigerant HFE-7100," *Int. J. Refrig.*, **33**, pp. 1221–1228.
- [44] Aktinol, E., and Dhir, V. K., 2012, "Numerical Simulation of Nucleate Boiling Phenomenon Coupled With Thermal Response of the Solid," *Microgravity Sci. Technol.*, **24**, pp. 255–265.

- [45] Wang, C. H., and Dhir, V. K., 1993, "Effect of Surface Wettability on Active Nucleation Site Density During Pool Boiling of Water on a Vertical Surface," *ASME J. Heat Transfer*, **115**(3), pp. 659–669.
- [46] Son, G., Ramanujapu, N., and Dhir, V. K., 2002, "Numerical Simulation of Bubble Merger Process on a Single Nucleation Site During Pool Nucleate Boiling," *ASME J. Heat Transfer*, **124**(1), pp. 51–62.
- [47] Mukherjee, A., and Dhir, V. K., 2004, "Study of Lateral Merger of Vapor Bubbles During Nucleate Pool Boiling," *ASME J. Heat Transfer*, **126**(6), pp. 1023–1039.
- [48] Abarajith, H. S., 2006, "Numerical Prediction and Experimental Validation of Pool Nucleate Boiling Heat Flux Under Variable Gravity Conditions," Ph.D. dissertation, University of California, Los Angeles, CA.
- [49] Son, G., and Dhir, V. K., 2008, "Numerical Simulation of Nucleate Boiling on a Horizontal Surface at High Heat Fluxes," *Int. J. Heat Mass Transfer*, **51**, pp. 2566–2582.
- [50] Basu, N., Warrier, G. R., and Dhir, V. K., 2002, "Onset of Nucleate Boiling and Active Nucleation Site Density During Subcooled Flow Boiling," *ASME J. Heat Transfer*, **124**(4), pp. 717–728.
- [51] Stephan, K., and Abdelsalam, M., 1980, "Heat Transfer Correlation for Natural Convection Boiling," *Int. J. Heat Mass Transfer*, **23**, pp. 73–87.
- [52] Son, G., and Dhir, V. K., 1997, "Numerical Simulation of Saturated Film Boiling on a Horizontal Surface," *ASME J. Heat Transfer*, **119**(3), pp. 525–533.
- [53] Brackbill, J. U., Kothe, D. B., and Zemach, C., 1992, "A Continuum Method for Modeling Surface Tension," *J. Comput. Phys.*, **100**, pp. 335–354.
- [54] Berenson, P. J., 1961, "Film-Boiling Heat Transfer From a Horizontal Surface," *ASME J. Heat Transfer*, **83**(3), pp. 351–356.
- [55] Klimentko, V. V., 1981, "Film Boiling on a Horizontal Plate—New Correlation," *Int. J. Heat Mass Transfer*, **24**, pp. 69–79.
- [56] Juric, D., and Tryggvason, G., 1998, "Computations of Boiling Flows," *Int. J. Multiphase Flow*, **24**, pp. 387–410.
- [57] Banerjee, D., and Dhir, V. K., 2001, "Study of Subcooled Film Boiling on a Horizontal Disc: Part I—Analysis," *ASME J. Heat Transfer*, **123**(2), pp. 271–284.
- [58] Banerjee, D., and Dhir, V. K., 2001, "Study of Subcooled Film Boiling on a Horizontal Disc: Part I—Experiments," *ASME J. Heat Transfer*, **123**(2), pp. 285–293.
- [59] Welch, S. W., and Wilson, J., 2000, "A Volume of Fluid Based Method for Fluid Flows With Phase Change," *J. Comput. Phys.*, **160**, pp. 662–682.
- [60] Welch, S. W. J., and Rachidi, T., 2002, "Numerical Computation of Film Boiling Including Conjugate Heat Transfer," *Numer. Heat Transfer Part B*, **42**, pp. 35–53.
- [61] Sakurai, A., Shioitsu, M., and Hata, K., 1990, "A General Correlation for Pool Film Boiling Heat Transfer From a Horizontal Cylinder to Subcooled Liquid: Part 2—Experimental Data for Various Liquids and Its Correlation," *ASME J. Heat Transfer*, **112**(2), pp. 441–450.